Vascular mapping of the human hippocampus using Ferumoxytol-enhanced MRI

Sagar Buch[a], **Yongsheng Chen**[b], **Pavan Jella**[a], **Yulin Ge**[c], **E. Mark Haacke**[a,*]

[a]Department of Radiology, Wayne State University, Detroit, MI, USA

[b]Department of Neurology, Wayne State University, Detroit, MI, USA

[c]Center for Biomedical Imaging, Department of Radiology, New York University School of Medicine, New York, NY, USA

Abstract

The hippocampus is a small but complex grey matter structure that plays an important role in spatial and episodic memory and can be affected by a wide range of pathologies including vascular abnormalities. In this work, we introduce the use of Ferumoxytol, an ultra-small superparamagnetic iron oxide (USPIO) agent, to induce susceptibility in the arteries (as well as increase the susceptibility in the veins) to map the hippocampal micro-vasculature and to evaluate the quantitative change in tissue fractional vascular density (FVD), in each of its subfields. A total of 39 healthy subjects (aged 35.4 ± 14.2 years, from 18 to 81 years old) were scanned with a high-resolution ($0.22 \times 0.44 \times 1$ mm^3) dual-echo SWI sequence acquired at four time points during a gradual increase in Ferumoxytol dose (final dose = 4 mg/kg). The volumes of each subfield were obtained automatically from the pre-contrast T_1-weighted data. The dynamically acquired SWI data were co-registered and adaptively combined to reduce the blooming artifacts from large vessels, preserving the contrast from smaller vessels. The resultant SWI data were used to segment the hippocampal vasculature and to measure the FVD ((volume occupied by vessels)/(total

*Corresponding author at: 3990 John R Street, MRI Concourse, Detroit, MI 48201.

volume)) for each subfield. The hippocampal fissure, along with the fimbria, granular cell layer of the dentate gyrus and cornu ammonis layers (except for CA1), showed higher micro-vascular FVD than the other parts of hippocampus. The CA1 region exhibited a significant correlation with age (R = −0.37, $p < 0.05$). demonstrating an overall loss of hippocampal vascularity in the normal aging process. Moreover, the vascular density reduction was more prominent than the age correlation with the volume reduction (R = −0.1, $p > 0.05$) of the CA1 subfield, which would suggest that vascular degeneration may precede tissue atrophy.

Keywords

Susceptibility weighted imaging; Hippocampus; Normal aging; Vasculature; USPIO

1. Introduction

The hippocampus is a small, complex grey matter structure located in the temporal lobe and is an important part of the limbic system (Eichenbaum, 2001). Many studies have reported that hippocampal atrophy is a neuroimaging hallmark of Alzheimer's disease (AD) (Jack et al., 2000, Albert et al., 2011). It is also impacted by socioeconomic disadvantage and individual hardships (Gianaros et al., 2017) in normal aging (Golomb et al., 1993, Lisman et al., 2017). As a result, quantitative data on the morphology of the hippocampus has become one of the important tools to evaluate cognitive decline in adulthood. The hippocampus is not a homogeneous structure but rather is composed of several subfields, specifically the cornu ammonis (CA) areas 1–4, granule cell layer of the dentate gyrus (GC-DG), molecular layer, subiculum, parasubiculum and presubiculum, fimbria, hippocampal fissure (HCfissure) and hippocampal tail (HCtail) (Duvernoy et al., 2013). Each subfield exhibits a distinct histological characteristic that appears to be affected by various neurodegenerative diseases (The Hippocampus Book). The reduced whole hippocampal and individual hippocampal subfield volumetric analyses have been correlated with multiple sclerosis (Sicotte et al., 2008), subjects with post traumatic stress disorder (O'Doherty et al., 2015), through hippocampal atrophy in AD (Jack et al., 2000) and in normal aging (Golomb et al., 1993). Notably, the hippocampal vasculature has increased vulnerability with a relatively poor vessel density, a limited number of arteries supplying the blood with scarce sources of anastomosis. The insufficiency of capillary density and afferent blood vessels is particularly apparent within the CA layers of the hippocampus, making them vulnerable to shortcomings in blood supply (Marinkovi et al., 1992). If a hypertensive vascular crisis (leading to regional hypoxia) were to occur, the nerve cells supplied by these vessels would succumb earlier than other regions in the brain where neighboring vascular units can help with reperfusion (Duvernoy et al., 2013, Scharrer, 1940). Earlier work has shown an age-dependent progressive loss of blood-brain-barrier integrity and capillary damage in the hippocampus, especially in CA1 (De Jong et al., 1999, Montagne et al., 2015). Post-mortem examinations have also found neuronal loss associated with the CA1 and the subiculum regions in vascular dementia patients with micro-vascular pathology (Kril et al., 2002). Some vascular pathologies affecting the hippocampus include: vascular dementia (Kril et al., 2002, van de Pol et al., 2011), subcortical ischemic vascular disease (Fein et al., 2000), transient global amnesia (Bartsch et al., 2006) and temporal lobe

epilepsy (Wieser, 2004). Therefore, it is quintessential to trace back the changes in cerebral micro-vasculature that can manifest early in pre-diagnostic stages. In fact, earlier studies have also demonstrated that normal aging is associated with reduced resting cerebral blood flow (Heo et al., 2010, Maass et al., 2015), showing that the vascular plasticity reduces with progressing age (Maass et al., 2015).

Hippocampal vessels are small (<1 mm) and difficult to visualize through in vivo imaging methods. Hence, restricting their examination so far to cadaver studies. In previous works, ultra-small superparamagnetic iron oxides (USPIO) have been used to induce susceptibility in the arteries (as well as an increase of the susceptibility in the veins over and above that caused by deoxyhemoglobin) (Buch et al., 2020, Liu et al., 2018, Shen et al., 2020). Although Ferumoxytol (a USPIO agent) introduces a strong T_1-shortening property to blood (Stoumpos et al., 2018, Toth et al., 2017), the primary contrast for this work is obtained through the T_2*-related signal loss, which helps reveal the micro-vasculature as demonstrated by a recent study on vascular abnormalities in multiple sclerosis lesions using susceptibility weighted imaging (SWI) (Buch et al., 2020). Hence, with this increase in susceptibility-related contrast comes the potential to make small sub-voxel vessels visible within the hippocampus. This method has been referred to as MICRO for 'Micro-vascular In-vivo Contrast Revealed Origins'. It employs multiple high-resolution dual-echo SWI sequences, acquired with a gradual increase in Ferumoxytol concentration. The strong negative contrast from the use of Ferumoxytol with SWI (which is a T_2* dominant approach) has significant advantages over T_1-weighted (T1W) imaging (which takes advantage of the strong T_1-shortening property of Ferumoxytol when very small doses are used). The T_2* decay can provide a much higher visualization of small structures than the small changes in signal caused by a reduction of T_1 in a vessel that occupies only a fraction of a voxel. This significantly improves the vessel enhancement on the gradient-recalled echo (GRE) magnitude (and consequently on the SWI data), as the magnetic susceptibility in the blood drastically increases due to the superparamagnetic property of Ferumoxytol (even at a low-dose of 4 mg/kg); which causes a strong local field inhomogeneity at the vessel boundary leading to extravascular dephasing. Hence, with the help of MICRO imaging, our goal is to extract the hippocampal micro-vasculature and obtain the vessel densities within its subfields. Determining the vascular density has significant value in characterizing healthy and diseased tissue and/or in deducing the degree of vulnerability for a structure to perfusion deficiency.

In this study, we have used high-resolution SWI data, in the presence of low-dose Ferumoxytol, and an optimized post-processing pipeline to map the intra-hippocampal micro-vasculature in healthy subjects. The increased susceptibility in the blood helped to reveal the subvoxel vessels, which were then compared with previous cadaver brain research on hippocampal vascular mapping (Duvernoy et al., 2013). The hippocampal subfields were segmented for each subject and the fractional vessel density (FVD) was measured across all the subfields as a function of age.

2. Methods

Data were acquired with local institutional review board approval at Wayne State University and all subjects signed an informed consent form. Thirty-nine (39) healthy subjects (aged 35.4 ± 14.2 years, from 18 to 81 years old, female = 20) were included in this study. All subjects were imaged on a 3T MRI scanner (Verio, Siemens Healthineers, Erlangen, Germany) with a 32-channel head coil. The imaging protocol included: T1W magnetization prepared rapid gradient echo (MPRAGE) and dual-echo SWI sequences, both acquired pre and post Ferumoxytol (Feraheme, AMAG Pharmaceuticals, Inc. Waltham, MA) administration. The subjects were scanned with a dual-echo SWI sequence at four time points: the first was acquired pre-contrast (Fe_0) and the remaining three were acquired post-contrast at intervals of 11 mins (Fe_1, Fe_2 and Fe_3) during a gradual increase in dose.

The final Ferumoxytol dose (4 mg/kg) was diluted with 60 ml of 0.9% sodium chloride (or normal saline) solution. Based on the subject-specific contrast volume after dilution, the intravenous administration rate was selected between the range of 150–200 ml/h to ensure a consistent delivery period of 21–23 min. The contrast administration was initiated at the start of the first post-contrast scan and care was taken that the entire contrast dose was administered to the subject before starting the last post-contrast scan (Fe_3).

The imaging parameters used for the SWI sequence were: TE1/TE2/TR = 7.5/15/27 ms, bandwidth = 181 Hz/pixel, acquisition plane = axial; with a voxel resolution = $0.22 \times 0.44 \times 1$ mm^3 (interpolated to $0.22 \times 0.22 \times 1$ mm^3 by zero filling k-space appropriately). Nineteen (19) subjects were acquired with a flip angle (FA) = 15° for Fe_0 and Fe_3 and 20° for Fe_1 and Fe_2, whereas the remaining cases were acquired with a FA of 12° for all time points. Similarly, the imaging parameters used for the T_1-MPRAGE sequence were: TE/TR = 3.4/1500 ms, inversion time = 900 ms, FA = 9°, bandwidth = 181 Hz/pixel, acquisition plane = axial; with a voxel resolution = $0.44 \times 0.44 \times 1$ mm^3. The generalized autocalibrating partially parallel acquisitions (GRAPPA) factor of 2 was used for the sequences with central 36 reference lines. Data from two subjects were not included in this study due to the motion during and between scans, which caused unwanted blurring of the smaller vessels; leaving data from thirty-seven (37) healthy controls that could be analyzed.

2.1. Post-processing of SWI data

The SWI images were generated using a homodyne high-pass filter (filter size = 128×128) of the phase images to generate a phase mask which was subsequently multiplied into the original magnitude images four times (Haacke et al., 2004). To correct potential inter-scan motion, all the post-contrast original magnitude and the processed SWI data as well as the pre- and post-contrast T_1 data were registered to the pre-contrast short TE (7.5 ms) magnitude data of the dual-echo SWI acquisition. The image registration was performed with the statistical parametric mapping (SPM) package (SPM12, Wellcome Centre for Human Neuroimaging, University College London, London, UK) in MATLAB (R2017b, MathWorks, Inc., Natick, MA, USA) by using normalized mutual information as the cost function and a 4th degree spline for interpolation (Collignon et al., 1995, Ashburner and Friston, 1997, Studholme et al., 1999). The transform parameters obtained from the short TE magnitude data registration were then applied to the SWI data. The registered SWI data

for the Fe_2 and Fe_3 time points (or SWI_{Fe2} and SWI_{Fe3}, respectively) were averaged to obtain an improved SWI data set ($SWI_{avg,2,3}$) with higher signal-to-noise ratio (SNR). The co-registered data were carefully reviewed by visually inspecting the shape and location of the large and small vessels on the registered SWI_{Fe2} and SWI_{Fe3} data in comparison with the $SWI_{avg,2,3}$. Finally, the dynamically collected SWI data from all time points were combined using the phase gradient based adaptive combination (SWI_{PGAC}) method described in a previous work (Buch et al., 2020). In brief, the regions with strong phase gradients (exhibiting strong blooming effects on the magnitude data) were identified using the Fe_2 timepoint phase data. A mask was then created of these regions and dilated over their immediate neighborhood (5 voxels). The regions included in this mask were adaptively combined with that of the previous time points exhibiting weaker blooming effects (first, with SWI of Fe_1timepoint and then with pre-contrast SWI). The registered pre-contrast T1W data was subtracted from the registered post-contrast T1W data to obtain a T_1 -enhancement map ($T_{1\,W\,MAP}$). The extent of small vessel enhancement was compared between the $T_{1\,W\,MAP}$ and the SWI_{Fe3} data.

2.2. Estimating the hippocampal vessel density

The maps of major arteries and veins were also obtained to determine the density of the primary vessels that supply and drain the blood from the hippocampus. An MR angiogram (MRA) of the major arteries was obtained using a non-linear subtraction (MRA_{nl}) of the long TE from the short TE of the pre-contrast magnitude data, with a subtraction constant of 1.5 (Ye et al., 2013). For the MR venogram (MRV), the pre-contrast quantitative susceptibility mapping (QSM) and R_2 * maps constituted two different representations of veins. R_2 * maps were calculated from the pre-contrast short and long TE magnitude data by performing a voxel-by-voxel mono-exponential fitting. QSM data were obtained from the pre-contrast timepoint using the following steps: the sophisticated harmonic artifact reduction for phase data (SHARP) method was first used to estimate the background field and remove it from the unwrapped phase (Schweser et al., 2011). The truncated k-space inverse filter approach with an iterative geometric constraint was then used to generate the QSM data, for each TE (Haacke et al., 2010, Tang et al., 2013). An averaged QSM was generated by an R_2 * -based weighted average of the individual echoes (Gharabaghi et al., 2020).

A third representation of veins only was generated by dividing the short TE Fe_1 magnitude data by the short TE Fe_0 magnitude data, to take advantage of the T_1 - shortening effect of Ferumoxytol. The T_1 - shortening effect from the low dose of Ferumoxytol leads to a larger increase in the venous signal since the arteries already have high intensity from the time-of-flight (TOF) effect (i.e., even for the pre-contrast data). This division then provides the third venous-only map. The three venous maps (pre-contrast QSM, R_2 * and the above-mentioned venous-only map) were then normalized to values between 0 and 1 and an average of these different MRV sources produced a high quality MRV, referred to as MRV_{avg} (for more details see ref. (Buch et al., 2020)).

In order to measure the vessel density, the Frangi vesselness filter was applied to the SWI_{PGAC} data (Frangi et al., 1998, Kroon, 2021). The vesselness measures were obtained

by setting the constants α, β and c to 0.5, 0.5 and 500, respectively, in Eq. 13 of Frangi et al., 1998 (Frangi et al., 1998), which allows the mapping of the geometric features into probability estimates of vesselness using the three eigenvalues of the Hessian matrix in order to differentiate the blood vessels. At each voxel, the vesselness was computed using the vessel size range of 0.2 to 1.2 voxels (incrementing the scale by 0.1) and the maximum vesselness response along its scale was selected. This was followed by setting a vesselness threshold of 2×10^{-4} to discard the unwanted background noise and by removing the islands with connectivity equal or smaller than 8 voxels in 3D in the binarized vesselness image to obtain the final micro-vasculature map (MVM). The process of obtaining the MVM is summarized in Figure S1. The MVM from SWI_{Fe2} and SWI_{Fe3}, using the same process described above, were obtained to validate the consistency of their FVD measures with the SWI_{PGAC}-derived FVD.

The MRV_{avg} and MRV_{nl} masks were used to discard any major vessels that were included in the MVM. The hippocampal subfields, including the parasubiculum, presubiculum, subiculum, cornu ammonis areas (CA1, CA2/3 composite, CA4), granule cell layer of the dentate gyrus, fimbria, molecular layer of hippocampus (MolLayer), hippocampal fissure and hippocampal tail, were generated from the registered pre-contrast T1W data using the hippocampus segmentation tool in Freesurfer (version 6.0.0, http://surfer.nmr.mgh.harvard.edu/) (Collins et al., 1994, Fischl et al., 2004, Fischl et al., 2002, Iglesias et al., 2015). Finally, the FVD was derived using: (volume occupied by vessels) / (total volume) for each segmented subfield from both hemispheres, where the 'volume occupied by vessels' was the number of non-zero voxels on the MVM image, and the 'total volume' was the number of voxels of the subfield mask. For quality assurance, visual inspection was performed to ensure the validity of the hippocampal segmentations since over-segmentation can be a problem when an automatic procedure is used (Wisse et al., 2021). In one subject, manual correction was performed when the hippocampal boundary was clearly incorrect on the T1W data. The location of the hippocampal fissure, which is one of the thinner layers, was confirmed by visually inspecting the overlap of its segmented mask on the hippocampal sulcus (exhibiting hypointense signal due to the presence of CSF in the sulcus) on the T1W data.

Manual contouring, data sorting and simple image manipulations were performed using SPIN-Research software (https://spintechimaging.com/products/research-software/). MATLAB was used for the post-processing steps, generating the maximum/minimum intensity projections (MIP/mIP), obtaining FVD values and performing statistical analyses. MRIcron (Rorden and Brett, 2000) (v1.0.2, https://www.nitrc.org/projects/mricron/) was used for visualizing the SWI_{PGAC} images with overlays of hippocampal subfields, MVM, MRV_{avg} and MRA_{nl}. Volview (VolView 3.4, Kitware, Clifton Park, NY, USA) was used for 3D rendering of the vascular network.

2.3. Statistical analyses

For a given subfield, an FVD measure that is more than three scaled median absolute deviations away from the median was labeled as an outlier and was removed from further analysis. The median FVDs for each hippocampal subfield across all subjects was then

calculated along with the interquartile range and the 95% confidence interval regions (and the values outside this confidence interval were considered outliers) to represent the FVDs for the cohort included in this study. Tukey's honest significant difference, with a significance level of $p < 0.05$, was used to perform multiple comparison of group means for 1) the total hippocampus FVDs derived from SWI_{Fe2}, SWI_{Fe3} and SWI_{PGAC} data; and 2) for the differences across the various hippocampal subfields. Pearson's correlation coefficient was obtained by comparing: 1) age with the FVD for each individual subfield and with the total FVD across the entire hippocampus; and 2) age with each individual subfield volume as well as the total hippocampal volume. The correlation was deemed significant if the p-value was lower than 0.05. Age-related correlation was further extended by comparing the slope and intercept of the FVD measures of the whole hippocampus for SWI_{Fe2}, SWI_{Fe3} and SWI_{PGAC} data. In order to test the equality of the age-related regression, the z-score was obtained by utilizing the slopes and the standard error in slopes of SWI_{PGAC} and SWI_{Fe3} data (with a significance of $|z| < 1.96$), as explained by Paternoster *et al.* (Paternoster et al., 1998).

3. Results

Figure S2 demonstrates the ability of the post-contrast SWI data to reveal the cerebral micro-vasculature (Figures S2D and S2E), whereas the $T_{1\ WMAP}$ was only able to highlight the major vessels (Figures S2C and S2F). Hence, with the presence of low-dose Ferumoxytol, there was a significant increase in the contrast for the hippocampal vascular network. However, the signal loss around the larger vessels was exacerbated due to the high susceptibility in the presence of Ferumoxytol. Hence, we employed the SWI_{PGAC} method, which provides more pristine delineation of the larger vessels and hence preserved the visibility of the smaller or subvoxel vessels.

Fig. 1A shows the whole brain vasculature that was enhanced after the administration of Ferumoxytol and then extracted using the proposed vesselness filtering steps to obtain MVM. The hippocampal vessels are highlighted in white (Fig. 1A) to better visualize their location and their progression from superior to inferior in the transverse plane. Fig. 1B shows the MIP for all the transverse slices covering the hippocampus, where the highlighted vessels demonstrate the entirety of the hippocampal vasculature. The mIP of SWI_{PGAC} and the MIP of the segmented intra-hippocampal vessels are separately displayed in Fig. 1C and D, respectively. The hippocampal vasculature on SWI_{Fe3}, $SWI_{avg,2,3}$ (the averaged image of SWI_{Fe2} and SWI_{Fe3}) and SWI_{PGAC} data are compared in Figure S3 for four selected subjects. Although the $SWI_{avg,2,3}$ provides an improvement in SNR over the SWI_{Fe3} data, the blooming artifact around the larger vessels that can be seen on both SWI_{Fe3} and $SWI_{avg,2,3}$ data. This vascular blooming was reduced after the adaptive combination (SWI_{PGAC}) of the dynamically acquired SWI data, which was then used to obtain the MVM, as seen in the bottom row of Figure S3. The $SWI_{avg,2,3}$ and SWI_{PGAC} data, for all subjects, are shown in supplementary Figures S4A and S4B, respectively. Consequently, the MIPs of the segmented intra-hippocampal vessels for all the subjects are displayed in supplementary Figure S5.

The slice-by-slice visualization of the MRA_{nl}, MRV_{avg}, SWI_{PGAC}, MVM and segmented hippocampal subfields for one subject are presented in the supplementary Figure S6. Fig. 2 shows the difference between the pre-contrast SWI and SWI_{PGAC} data in visualizing the micro-vasculature across four selected subjects. The intra-hippocampal and superficial major arteries and veins (mapped through the MRA_{nl} and MRV_{avg} data, respectively) are used as an overlay in the third column to better visualize the major vessels penetrating and draining the hippocampus. The entire visible vascular network, including the MVM, that was segmented using the MICRO protocol is displayed in the fourth column, overlayed on the segmented mask of the hippocampus (see also the supplemental Video 1 illustrating the hippocampal vasculature in 3D). Fig. 3 compares the cadaver brain data adapted from Duvernoy et al. (Duvernoy et al., 2013) (Fig. 3A) with our *in vivo* results in mapping the subvoxel vessels of the hippocampus. The dense vascular layer of the fimbrio dentate sulcus (blue arrows) within the hippocampus, as shown in the cadaver brain data, can be seen on our *in vivo* results with the help of Ferumoxytol and the proposed processing steps. Similarly, the subependymal intra-hippocampal veins (red arrows) branching out of the major fimbrio dentate sulcus vein were visualized on the segmented vessel map.

The FVD measures for all the subfields from the SWI_{PGAC} data are shown in Fig. 4A and significance of the differences in their means are listed in Table S1. The HCfissure, along with the fimbria, granular cell layer of the dentate gyrus and cornu ammonis layers (except for CA1), showed higher micro-vascular FVD than the other parts of hippocampus. On the other hand, the FVD of the major arteries (Fig. 4B) and major veins (Fig. 4C) was higher in the HCfissure and CA2/3 composite regions; suggesting a stronger probability that these regions serve as the entry/exit area for the penetrating arteries and draining veins. As these areas also showed a high micro-vascular FVD, we can deduce that the transition of macro-vasculature into the smaller branches occurs in these regions. The mean FVD values for all subfields and total hippocampal FVD are listed in Table 1. These FVD obtained from the SWI_{PGAC} data were lower than that of the Fe_2 and, especially, Fe_3 SWI data (supplementary Figure S7A). This was due to the reduction in blooming artifacts for SWI_{PGAC} that will otherwise overestimate the FVD, as seen by the Fe_3 values.

Statistical results of the FVD measures for each individual hippocampal subfield and the total hippocampal FVD in correlation with age are illustrated in Fig. 5. There was a weak positive correlation for the FVD of GC-DG and HCfissure with age, whereas the FVD measures of CA4 and fimbria showed no or negligible correlation. More specifically, CA1 exhibited a significant correlation with age (R = −0.37, $p < 0.05$). In addition, the age-related correlation of the FVD measures (from the whole hippocampus) obtained from SWI_{Fe2} (R = −0.26) and SWI_{Fe3} (R = −0.29) were found to be consistent with the SWI_{PGAC}-derived measures (R = −0.31) demonstrating the reproducibility of the MVM masks (Figure S7B). Furthermore, the slope and the intercept of FVD as a function of age (in years) were: for SWI_{Fe2}, FVD = −0.0006•age + 0.13; for SWI_{Fe3}, FVD = −0.0005•age + 0.14 and for SWI_{PGAC}, FVD = −0.0005•age + 0.11; which demonstrates that the slopes were not significantly different (|z| < 1.96) across the three types of SWI data, only the intercept for SWI_{PGAC} was lower than others due to reduced blooming, as mentioned earlier.

The tissue volume changes showed a weakly negative or lack of correlation as a function of age (Figure S8). The total hippocampal FVD showed a negative correlation with age, demonstrating an overall loss of hippocampal vascularity in the normal aging process ($R = -0.31$), whereas the total hippocampus volume was negatively correlated with age ($R = -0.10$), but both these correlations were not statistically significant ($p > 0.05$).

4. Discussion

In this paper, we have successfully mapped the micro-vasculature of the hippocampus by utilizing the high-resolution MICRO protocol data, which acquires SWI data at multiple timepoints in the presence of low-dose (4 mg/kg) Ferumoxytol. The extracted hippocampal vessel map, from the SWI_{PGAC} data, allowed us to calculate the FVD in each of the intra-hippocampal subfields, which showed that CA1, subiculum and hippocampal tail exhibited lower FVD than the other sub-fields. Although the CA1 tissue volume was independent of age (Figure S6), it showed a significant ($p < 0.05$) age-dependent reduction in FVD (Fig. 5) (for FVD: $R = -0.37$, $p < 0.05$ vs. for CA1 volume: $R = -0.10$, $p > 0.05$).

Convetionally, SWI is known as a powerful tool to image the sub-voxel veins. However, it is insensitive to arteries in their natural form due to the low level of deoxygenated hemoglobin in arterial blood, which results in no susceptibility contrast between arteries and the surrounding tissue. By administering a strongly paramagnetic agent, Ferumoxytol, SWI was able to detect both arteries and veins; and its sensitivity to detect sub-voxel objects increased tremendously. The reason for choosing a higher filter size than the conventional 96×96 filter size for SWI processing was mainly to adapt the filter strength with the large inplane matrix size that this study uses (1024×832), whereas the conventional filter is used for matrix sizes of 512×512 or lower (Haacke et al., 2009). Hence, utilizing the 96×96 filter will not have the same vascular enhancement on our larger matrix data. Figure S2 further demonstrates the superiority of the high-resolution SWI data (due to both the increased dephasing/blooming artifact as well as to the special processing from SWI that uses the phase information) over the conventionally used T1W data that takes advantage of the strong T_1-shortening property of Ferumoxytol in enhancing the cerebral micro-vasculature. With the help of the MICRO imaging protocol, and using a resolution of 0.22×0.44×1 mm^3 (Albert et al., 2011), we were able to detect small vessels on the order of 100 μm. In principle, it is possible to acquire the data with a higher resolution, but acquisition time would be increased and SNR reduced thereby hindering their visualization, especially in the center of the brain. With strong blooming effects, Ferumoxytol enhanced SWI can circumvent both insufficient spatial resolution and insufficient contrast for very small arterial and venous vessels, thus offering the capability of imaging micro-vessels. Interestingly, the anisotropic aspect ratio of 1:4 [in-plane : through-plane resolution] is favored as it results in a stronger signal cancellation, due to the phase dispersion across a larger voxel size and the relative increase in SNR (Xu and Haacke, 2006); making it easier to extract the vasculature for the FVD measures. Higher resolution would be possible using 7T scanners and faster imaging with wave-controlled aliasing in parallel imaging (CAIPI) SWI could allow a reduction of scan time to just 5 to 10 minutes with a resolution of 0.22×0.22×1 mm^3 (Albert et al., 2011) (Bilgic et al., 2015, Conklin et al., 2019).

Another widely utilized method for vascular imaging is TOF that inherently takes advantage of the fresh spins arriving into the imaging slab or the 3D volume, which generates a strong hyperintense signal for the vessels (most likely the arteries) as compared to the surrounding stationary tissues such as grey- and white-matter. Moreover, it does not need any T_1 - or T_2 * shortening contrast agent, such as the one used in this study. Hence, TOF-based MR angiography (MRA) provides a robust way to obtain a map of major arteries, as shown in our study using a 3T scanner. Indeed, the utilization of higher field strength (7T) has been shown to be extremely useful in improving the visualization of the arterial vasculature (Vockert et al., 2021, Perosa et al., 2020, Spallazzi et al., 2019). On the other hand, the presence of Ferumoxytol strongly alters the magnetic properties of the blood (both T_1 and T_2 *), which dominates the TOF effect, making it possible to visualize the smaller vessels. With the help of GRE acquisition, a relatively higher TE (15 ms) and SWI processing, the CNR of the subvoxel vessels is further improved. This has been shown in Fig. 2, where our implementation of TOF-based MRA (i.e., MRA_{nl}) from the pre-contrast high-resolution SWI data high-lights the large arteries (red) such as PCA (2 – 3 mm) and AChA (0.7 – 2 mm) to smaller branches of PCA (1 mm) (Spallazzi et al., 2019); whereas the smaller subvoxel vasculature that include the straight hippocampal arteries (50 – 330 μm) (Marinkovi et al., 1992), intrahippocampal arteries and subependymal veins (50 – 200 μm) (Duvernoy et al., 2013, Marinkovi et al., 1992) could only be revealed in the presence of Ferumoxytol (4 mg/kg).

Although the vesselness filter can reasonably well extract the vessels, the SNR in the SWI data affects how well the background noisy voxels can be suppressed and a lower SNR can deteriorate the ability to segment the vessels, especially the smaller ones. On the other hand, the larger vessels have strong contrast on the post-contrast data, that can be easily extracted using the vesselness process. However, larger vessels are exaggerated in terms of their size and that can lead to an overestimate of the vessel density for regions with a major vessel passing through them. Hence, to address both these issues, we have used the SWI_{PGAC} combination method that takes advantage of the SWI data acquired over multiple timepoints with increasing concentrations of Ferumoxytol. The SWI_{PGAC} process averages the last two timepoint magnitude datasets and then multiplies it with the phase mask of the last timepoint; this helps to improve the SNR and gives better segmentation of the smaller vessels. Further, the SWI_{PGAC} method also adaptively combines the SWI data with increasing vessel contrast, by replacing the regions with strong phase gradients (such as at the large vessel boundaries at the last post-contrast timepoint) with that of the previous timepoint (i.e., at a lower Ferumoxytol concentration) SWI signal (Buch et al., 2020). This process helps to reduce the aforementioned exaggeration in the large vessel volume due to blooming artifacts and avoids overestimating the FVD.

Cornu ammonis layers (CA1, CA2/3 and CA4) are known to be pre-dominantly supplied by the PCA and its branches (Erdem et al., 1993, Hens and Van den Bergh, 1977, Muller and Shaw, 1965). The lower FVD in the CA1 can be partly explained through the recent work that studied the distance of major arteries from the different hippocampal subfields, which showed that the distance was highest from CA1 than other layers of the cornu ammonis (Haast et al., 2021). The same study also analyzed the perfusion data across the different cornu ammonis layers, where the perfusion was higher in CA2, CA3 and CA4 as compared

to CA1. Although the perfusion measure includes the capillaries as well, the FVD results from the post-contrast data included in our work is in agreement with their findings. The presence of the superparamagnetic contrast agent in the blood does make it possible to determine the local relative cerebral blood volume (rCBV) of the underlying capillary bed by using the pre- and post-contrast magnitude data, as shown by earlier studies (Yablonskiy and Haacke, 1994, Kuppusamy et al., 1996). However, due to the relatively low signal change induced by the hippocampal capillary bed with the current TEs and the noise level in the images (a consequence of high spatial resolution), the rCBV measures were deemed low in sensitivity and were not included in this work. Further investigation in improving the SNR of the data and/or using MICRO imaging at 7T could make it possible to quantitatively measure the capillary density or local rCBV.

The inability to provide adequate reperfusion has been associated with the hippocampus in the past due to its increase vascular vulnerability and to the reduced sources of anastomosis in case of a hypoxicischemic event; this may explain the age-dependent FVD reduction in CA1 subfield of hippocampus. We observed a significant reduction in the vascular density within the CA1 (R = −0.37, $p < 0.05$) with age (Fig. 5). This reduction of FVD with age is agreement with previous studies (Heo et al., 2010, Maass et al., 2015). Additionally, the entire hippocampus showed a reduction in vessel density with age ($p > 0.05$, Fig. 5). Interestingly, the CA1 territory showed no volume dependence with age (R = −0.1, $p > 0.05$). This suggests that the CA1 could be a potential source or starting territory of vascular atrophy in the hippocampus. The earlier studies on the human cadaver brains with vascular ink and methylmethacrylate injection showed that the CA1 sector (or Sommer's sector) is poorly vascularized and was found to be most sensitive to ischemia as compared to the other layers of the cornu ammonis (i.e., CA2 and CA3) and the rest of the hippocampal regions (Duvernoy et al., 2013, Marinkovi et al., 1992). Pyramidal neurons located in the CA1 region were also observed to be highly vulnerable to damage from hypoxia-ischemia (Kreisman et al., 2000). Furthermore, recent studies have measured glucose metabolism using positron emission tomography (PET) imaging in hippocampal subdivisions in healthy and AD patients, and have demonstrated lower metabolism and increased tissue atrophy in CA1 for AD patients (Choi et al., 2018, Carlson et al., 2020). Due to the coupling between blood oxygenation and glucose metabolism (Kucyi et al., 2018, Nir et al., 2007, Fox et al., 1988), we suspect that this reduction in glucose metabolism for AD patients could be correlated with the vascular density reduction within the CA1 subfield.

There are a few limitations of our study. First, there is a lack of subjects with diseases that directly affect the hippocampus such as AD and epilepsy. However, this pilot study on healthy subjects is essential for future studies on diseased brains in determining whether there is a loss of local vascular density in the hippocampus compared to healthy subjects. Second, a better extraction of the vessels could be possible in the future if the resolution could be pushed to $0.22 \times 0.22 \times 1$ mm^3 (Albert et al., 2011). As mentioned earlier, this is possible at 7T and with newer faster imaging techniques such as wave-CAIPI SWI allowing not only the increased spatial resolution but also temporal resolution with gradually increasing contrast concentration.

Third, the flip angles were modified from 15° for Fe_0 and Fe_3 time-points and 20° for Fe_2 and Fe_3 timepoints to 12° for all timepoints after acquiring data for 19 subjects. The decision to choose a higher FA (15° for Fe_0 and Fe_3 and 20° for Fe_1 and Fe_2) during the initial stages of the study was based on the goal to suppress the background tissues (white and grey matter), which should have helped in improving the vascular contrast and, hence, provide a better means of extracting the vessels for vessel density measurements. However, the tissue suppression was not as substantial as expected and the overall SNR for the original magnitude images for the higher FAs (especially for the Fe_1 and Fe_2 time-points) was not optimal. Consequently, a FA closer to the Ernst angle for gray matter was chosen and was kept constant across all pre- and post-contrast timepoints, for the remainder of the study. This modification leads to only very slight changes in the signal behaviour, which will not affect the vascular signal detection on the post-USPIO SWI data across the different subjects.

Fourth, this study employs the automatic segmentation tool to extract the hippocampal subfields from the registered T1W data. Although the manual segmentation of the subfields is considered the gold-standard, the auto-segmentation tool has shown good agreement with the manually segmented masks using an *ex vivo* study (Iglesias et al., 2015). However, there have been concerns about the accuracy of this method in the past, in particular, when the T1W data with lower resolution (~1 mm^3) were used to obtain the subfield masks (Wisse et al., 2021). In order to address this issue, the T1W data in our protocol was acquired with a higher resolution ($0.44 \times 0.44 \times 1$ mm^3) and was further interpolated to $0.22 \times 0.22 \times 1$ mm^3 to match the resolution of the high-resolution SWI data. Another concern about the segmentation tool was its reduced accuracy on older subjects (> 70 years) (Wenger et al., 2014). Their analysis was done on an earlier version of the tool (Freesurfer v5.3) and the updated version (Freesurfer v6.0) has shown improved accuracy with the incorporation of the *ex vivo* training and validation (Iglesias et al., 2015). Moreover, the intermediate steps involved in obtaining the automatic hippocampal segmentations have been validated using histological and manual measurements (Salat et al., 2004, Rosas et al., 2002, Kuperberg et al., 2003). The morphometric processes involved have also been analyzed through test-retest reliability across different manufacturers and field strengths (Brown et al., 2020, Worker et al., 2018). Nevertheless, we concede that higher resolution (and ideally isotropic, afforded through higher field strengths and better SNR) would make it possible to further improve the specificity of the subtle subfield changes and provide a better visual examination of each subfield in case a manual correction is required. Fifth, the subjects were administered with a fixed dose of 4 mg/kg, but the inter-subject differences in liver function may affect the overall contrast present in the blood. This may cause a bias in the vascular contrast, but has been minimized since we acquired the data right after the administration, given the half-life of Ferumoxytol ~ 15 hours.

Moreover, the FVD values measured on Fe_2 were slightly lower than that of for the Fe_3 timepoint, but they showed no significant different in the distributions FVDs across the whole hippocampus (Figure S7A). Nevertheless, the inclusion of the Fe_2 in the $SWI_{avg,2,3}$ data to produce the final SWI_{PGAC} results could potentially reduce the contrast for the smaller vessels. The individual SWI_{Fe2} and SWI_{Fe3} data possess increased blooming around the larger (even several medium vessels, as shown in Figures S3 and S4), which has

overestimated final FVD results (as shown in Fig. 5A and a reduce intercept for SWI_{PGAC}-derived FVD vs. age correlation in 5B). Nevertheless, the age correlation of the FVDs from all three types of SWI data showed that slopes ($|z| < 1.96$, Figure S7B), demonstrating the reproducibility of the proposed vessel extraction process.

Due to the higher imaging resolution used in this study, the SWI_{Fe2} and SWI_{Fe3} data also exhibit a lower SNR than the images that are obtained by combining them ($SWI_{avg,2,3}$ and SWI_{PGAC}). In our experience, this reduced SNR makes it difficult to completely discard noise pixels picked up by the vesselness approach (which incorrectly tends to increase the FVD values). The trade off of increasing the overall threshold on the final vesselness image is that we will discard voxels that belong to smaller vessels. Therefore, for this study, we chose to use the SWI_{PGAC} data (derived from $SWI_{avg,2,3}$) as opposed to SWI_{Fe3} in order to reduce the bias due to blooming artifacts and lower image quality. While the study provides a drastic improvement in vascular contrast, the process of administrating the contrast agent and a relatively long acquisition time could make it difficult to implement in older subjects or patients that are prone to motion. It should be noted that, in the presence of Ferumoxytol (4 mg/kg), and using the proposed high-resolution ($0.22 \times 0.44 \times 1$ mm^3) SWI-based micro-vasculature enhancement, one can expect the detection of vessels with sizes at the order of 100 μm [22,23]. This should be taken into consideration before correlating the measured FVD values obtained from the MICRO approach with other techniques that may, for example, include capillary contributions. Finally, this study involved imaging subjects with a limited age , mostly from 20 to 60 years of age. To better understand the effect of aging on the vascular density in different regions of hippocampus, data from more elder subjects (>60 years) should be collected.

5. Conclusion

In this work, we demonstrated the utility of low dose Ferumoxytol in imaging the micro-vasculature of the hippocampus using high-resolution SWI at 3T. The hippocampal fissure, along with the fimbria, granular cell layer of the dentate gyrus and cornu ammonis layers (except for CA1), showed higher micro-vascular FVD than the other parts of hippocampus. On the other hand, the FVD of major arteries and major veins was higher in the hippocampal fissure and CA2/3 composite regions, suggesting a stronger probability that these regions serve as the entry/exit area for the penetrating arteries and draining veins. There was a significant negative correlation of the CA1 FVD with age. This vascular density reduction was more prominent than the volume reduction suggesting that vascular atrophy may precede reductions in tissue volume. Mapping the vasculature of the brain and hippocampus in particular has immediate implications for understanding the etiology of many neurovascular and neurodegenerative diseases.

Supplementary Material

Refer to Web version on PubMed Central for supplementary material.

Acknowledgements

Abbreviations

CA1, CA2/3 composite, CA4

Cornu ammonis areas (hippocampus sub-fields)

CAIPI

Controlled aliasing in parallel imaging

FA

Flip angle

Fe_0

Pre-contrast timepoint

Fe_1, Fe_2, Fe_3

Post-contrast timepoints with gradually increasing ferumoxytol concentration

FVD

Fractional vessel density

GC-DG

Granule cell layer of the dentate gyrus (hippocampus subfield)

GRE

Gradient-recalled echo

HCfissure

Hippocampal fissure (hippocampus sub-field)

HCtail

Hippocampal tail (hippocampus subfield)

MICRO

Micro-vascular In-vivo Contrast Revealed Origins

MIP

Maximum intensity projection

mIP

Minimum intensity projection

MolLayer

Molecular layer of hippocampus (hippocampus subfield)

MPRAGE

Magnetization prepared rapid gradient echo

MRA

MR angiogram

MRA_{nl}

MRA obtained using non-linear subtraction method

MRV

MR venogram

MRV_{avg}

Averaged MRV

MVM

Micro-vasculature map

QSM

Quantitative susceptibility mapping

SHARP

Sophisticated harmonic artifact reduction for phase data

SNR

Signal-to-noise ratio

SPM

Statistical parametric mapping

SWI

Susceptibility weighted imaging

$SWI_{avg,2,3}$

Averaged image of SWI_{Fe2} and SWI_{Fe3}

SWI_{Fe2}

SWI of Fe_2 post-contrast timepoint

SWI_{Fe3}

SWI of Fe_3 post-contrast timepoint

SWI_{PGAC}

Dynamically combined SWI using the phase gradient-based adaptive combination method

TE
Echo time

TOF
Time-of-flight

TR
Repetition time

USPIO
Ultra-small superparamagnetic iron oxide

References

Albert MS, et al. 2011. The diagnosis of mild cognitive impairment due to Alzheimer's disease: recommendations from the National Institute on Aging-Alzheimer's Association workgroups on diagnostic guidelines for Alzheimer's disease. Alzheimers Dement. 7, 270–279. [PubMed: 21514249]

Ashburner J, Friston K, 1997. Multimodal image coregistration and partitioning-a unified framework. Neuroimage 6, 209–217. [PubMed: 9344825]

Bartsch T, et al. 2006. Selective affection of hippocampal CA-1 neurons in patients with transient global amnesia without long-term sequelae. Brain 129, 2874–2884. [PubMed: 17003071]

Bilgic B, et al. 2015. Wave-CAIPI for highly accelerated 3D imaging. Magn. Reson. Med 73, 2152–2162. [PubMed: 24986223]

Brown EM, et al. 2020. Test-retest reliability of FreeSurfer automated hippocampal subfield segmentation within and across scanners. Neuroimage 210, 116563. [PubMed: 31972281]

Buch S, et al. 2020. Subvoxel vascular imaging of the midbrain using USPIO-Enhanced MRI. Neuroimage 220, 117106. [PubMed: 32615253]

Buch S, et al. 2020. Revealing vascular abnormalities and measuring small vessel density in multiple sclerosis lesions using USPIO. NeuroImage 102525. doi:10.1016/j.nicl.2020.102525. [PubMed: 33338965]

Carlson ML, et al. 2020. Simultaneous FDG-PET/MRI detects hippocampal subfield metabolic differences in AD/MCI. Sci. Rep 10, 12064. [PubMed: 32694602]

Choi EJ, et al. 2018. Glucose Hypometabolism in Hippocampal Subdivisions in Alzheimer's Disease: A Pilot Study Using High-Resolution ^{18}F-FDG PET and 7.0-T MRI. J. Clin. Neurol 14, 158–164. [PubMed: 29629524]

Collignon A, et al. 1995. Automated multi-modality image registration based on information theory. Bizais .

Collins DL, Neelin P, Peters TM, Evans AC, 1994. Automatic 3D intersubject registration of MR volumetric data in standardized Talairach space. J. Comput. Assist. Tomogr 18, 192–205. [PubMed: 8126267]

Conklin J, et al. 2019. Validation of highly accelerated wave-CAIPI SWI compared with conventional SWI and T2* -weighted gradient recalled-echo for routine clinical brain MRI at 3T. AJNR Am. J. Neuroradiol 40, 2073–2080. [PubMed: 31727749]

De Jong GI, et al. 1999. Cerebral hypoperfusion yields capillary damage in the hippocampal CA1 area that correlates with spatial memory impairment. Neuroscience 91, 203–210. [PubMed: 10336071]

Duvernoy HM, Cattin F, Risold P-Y, 2013. The Human Hippocampus: Functional Anatomy, Vascularization and Serial Sections with MRI. Springer-Verlag doi:10.1007/978-3-642-33603-4.

Eichenbaum H, 2001. The hippocampus and declarative memory: cognitive mechanisms and neural codes. Behav. Brain Res 127, 199–207. [PubMed: 11718892]

Erdem A, Ya, argil G, Roth P, 1993. Microsurgical anatomy of the hippocampal arteries. J. Neurosurg 79, 256–265. [PubMed: 8331410]

Fein G, et al. 2000. Hippocampal and cortical atrophy predict dementia in subcortical ischemic vascular disease. Neurology 55, 1626–1635. [PubMed: 11113215]

Fischl B, et al. 2002. Whole brain segmentation: automated labeling of neuroanatomical structures in the human brain. Neuron 33, 341–355. [PubMed: 11832223]

Fischl B, et al. 2004. Automatically parcellating the human cerebral cortex. Cereb. Cortex 14, 11–22 . [PubMed: 14654453]

Fox PT, Raichle ME, Mintun MA, Dence C, 1988. Nonoxidative glucose consumption during focal physiologic neural activity. Science 241, 462–464. [PubMed: 3260686]

Frangi A, Niessen W, Vincken K, Viergever M, 1998. Multiscale vessel enhancement filtering. In: Medical Image Computing and Computer Assisted Intervention vol. 1496 of Lecture Notes in Computer Science, pp. 130–137.

Gharabaghi S, et al. 2020. Multi-echo quantitative susceptibility mapping for strategically acquired gradient echo (STAGE) imaging. Front. Neurosci 14, 581474. [PubMed: 33192267]

Gianaros PJ, et al. 2017. Community socioeconomic disadvantage in midlife relates to cortical morphology via neuroendocrine and cardiometabolic pathways. Cereb. Cortex 27, 460–473. [PubMed: 26498832]

Golomb J, et al. 1993. Hippocampal atrophy in normal aging. An association with recent memory impairment. Arch. Neurol 50, 967–973. [PubMed: 8363451]

Haacke EM, Xu Y, Cheng Y-CN, Reichenbach JR, 2004. Susceptibility weighted imaging (SWI). Magn. Reson. Med 52, 612–618 [PubMed: 15334582]

Haacke E, Mittal S, Wu Z, Neelavalli J, Cheng Y-CN, 2009. Susceptibility-weighted imaging: technical aspects and clinical applications, part 1. Am. J. Neuroradiol 30, 19–30. [PubMed: 19039041]

Haacke EM, Tang J, Neelavalli J, Cheng YCN, 2010. Susceptibility mapping as a means to visualize veins and quantify oxygen saturation. J. Magn. Reson. Imaging 32, 663–676. [PubMed: 20815065]

Haast RAM, et al. 2021. Delineating perfusion and the effects of vascularisation patterns across the hippocampal subfields at 7T. In: Proceedings of the 20th Annual Meeting of ISMRM.

Hens L, Van den Bergh R, 1977. Vascularization and angioarchitecture of the human pes hippocampi. Eur. Neurol 15, 264–267. [PubMed: 913439]

Heo S, et al. 2010. Resting hippocampal blood flow, spatial memory and aging. Brain Res. 1315C (119).

Iglesias JE, et al. 2015. A computational atlas of the hippocampal formation using ex vivo, ultra-high resolution MRI: Application to adaptive segmentation of in vivo MRI. Neuroimage 115, 117–137. [PubMed: 25936807]

Jack CR, et al. 2000. Rates of hippocampal atrophy correlate with change in clinical status in aging and AD. Neurology 55, 484–489. [PubMed: 10953178]

Kreisman NR, Soliman S, Gozal D, 2000. Regional differences in hypoxic depolarization and swelling in hippocampal slices. J. Neurophysiol 83, 1031–1038. [PubMed: 10669514]

Kril J, Patel S, Harding A, Halliday G, 2002. Patients with vascular dementia due to microvascular pathology have significant hippocampal neuronal loss. J. Neurol. Neurosurg. Psychiatry 72, 747–751. [PubMed: 12023418]

Kroon D-J, 2021. Hessian based Frangi Vesselness Filter https://www.mathworks.com/matlabcentral/fileexchange/24409-hessian-based-frangi-vesselness-filter.

Kucyi A, et al. 2018. Intracranial Electrophysiology Reveals Reproducible Intrinsic Functional Connectivity within Human Brain Networks. J. Neurosci 38, 4230–4242. [PubMed: 29626167]

Kuperberg GR, et al. 2003. Regionally localized thinning of the cerebral cortex in schizophrenia. Arch. Gen. Psychiatry 60, 878–888. [PubMed: 12963669]

Kuppusamy K, Lin W, Cizek GR, Haacke EM, 1996. vivo regional cerebral blood volume: quantitative assessment with 3D T1-weighted pre- and postcontrast MR imaging. Radiology 201, 106–112. [PubMed: 8816529]

Lisman J, et al. 2017. Viewpoints: how the hippocampus contributes to memory, navigation and cognition. Nat. Neurosci 20, 1434–1447. [PubMed: 29073641]

Liu S, Brisset J-C, Hu J, Haacke EM, Ge Y, 2018. Susceptibility weighted imaging and quantitative susceptibility mapping of the cerebral vasculature using ferumoxytol. J. Magn. Reson. Imaging 47, 621–633. [PubMed: 28731570]

Maass A, et al. 2015. Vascular hippocampal plasticity after aerobic exercise in older adults. Mol. Psychiatry 20, 585–593. [PubMed: 25311366]

Marinkovi S, Milisavljevi M, Puskas L, 1992. Microvascular anatomy of the hippocampal formation. Surg. Neurol 37, 339–349. [PubMed: 1631758]

Montagne A, et al. 2015. Blood-brain barrier breakdown in the aging human hippocampus. Neuron 85, 296–302. [PubMed: 25611508]

Muller J, Shaw L, 1965. Arterial vascularization of the human hippocampus. 1. Extracerebral relationships. Arch. Neurol 13, 45–47. [PubMed: 14314273]

Nir Y, et al. 2007. Coupling between neuronal firing rate, gamma LFP, and BOLD fMRI is related to interneuronal correlations. Curr. Biol 17, 1275–1285. [PubMed: 17686438]

O'Doherty DCM, Chitty KM, Saddiqui S, Bennett MR, Lagopoulos J, 2015. A systematic review and meta-analysis of magnetic resonance imaging measurement of structural volumes in posttraumatic stress disorder. Psychiatry Res. 232, 1–33. [PubMed: 25735885]

Paternoster R, Brame R, Mazerolle P, Piquero A, 1998. Using the correct statistical test for the equality of regression coefficients. Criminology 36, 859–866.

Perosa V, et al. 2020. Hippocampal vascular reserve associated with cognitive performance and hippocampal volume. Brain 143, 622–634. [PubMed: 31994699]

Rorden C, Brett M, 2000. Stereotaxic display of brain lesions. Behav. Neurol 12, 191–200. [PubMed: 11568431]

Rosas HD, et al. 2002. Regional and progressive thinning of the cortical ribbon in Huntington's disease. Neurology 58, 695–701. [PubMed: 11889230]

Salat DH, et al. 2004. Thinning of the cerebral cortex in aging. Cereb. Cortex 14, 721–730. [PubMed: 15054051]

Scharrer E, 1940. Vascularization and vulnerability of the cornu ammonis in the opossum. Arch. Neurol. Psychiatry 44, 483–506.

Schweser F, Deistung A, Lehr BW, Reichenbach JR, 2011. Quantitative imaging of intrinsic magnetic tissue properties using MRI signal phase: an approach to in vivo brain iron metabolism? Neuroimage 54, 2789–2807. [PubMed: 21040794]

Shen Y, et al. 2020. Detecting sub-voxel microvasculature with USPIO-enhanced susceptibility-weighted MRI at 7 T. Magn. Reson. Imaging 67, 90–100. [PubMed: 31911199]

Sicotte NL, et al. 2008. Regional hippocampal atrophy in multiple sclerosis. Brain 131, 1134–1141. [PubMed: 18375977]

Spallazzi M, et al. 2019. Hippocampal vascularization patterns: A high-resolution 7 Tesla time-of-flight magnetic resonance angiography study. NeuroImage: Clinical 21, 101609. [PubMed: 30581106]

Stoumpos S, et al. , 2018. Ferumoxytol-enhanced magnetic resonance angiography for the assessment of potential kidney transplant recipients. Eur. Radiol 28, 115–123. [PubMed: 28677065]

Studholme C, Hill DLG, Hawkes DJ, 1999. An overlap invariant entropy measure of 3D medical image alignment. Pattern Recognit. 32, 71–86.

Tang J, et al. 2013. Improving susceptibility mapping using a threshold-based K-space/image domain iterative reconstruction approach. Magn. Reson. Med 69, 1396–1407. [PubMed: 22736331]

The Hippocampus Book. (Oxford University Press, 2006). doi:10.1093/acprof:oso/9780195100273.001.0001.

Toth GB, et al. 2017. Current and potential imaging applications of ferumoxytol for magnetic resonance imaging. Kidney Int. 92, 47–66. [PubMed: 28434822]

van de Pol L, Gertz H-J, Scheltens P, Wolf H, 2011. Hippocampal atrophy in subcortical vascular dementia. Neurodegener. Dis 8, 465–469. [PubMed: 21613775]

Vockert N, et al. 2021. Hippocampal vascularization patterns exert local and distant effects on brain structure but not vascular pathology in old age. Brain Commun 3, fcab127. [PubMed: 34222874]

Wenger E, et al. 2014. Comparing manual and automatic segmentation of hippocampal volumes: reliability and validity issues in younger and older brains. Hum. Brain Mapp 35, 4236–4248. [PubMed: 24532539]

Wieser H-GILAE Commission on Neurosurgery of Epilepsy, 2004. ILAE Commission Report. Mesial temporal lobe epilepsy with hippocampal sclerosis. Epilepsia 45, 695–714. [PubMed: 15144438]

Wisse LEM, et al. 2021. Hippocampal subfield volumetry from structural isotropic 1 mm3 MRI scans: a note of caution. Hum. Brain Mapp 42, 539–550. [PubMed: 33058385]

Worker A, et al. 2018. Test-retest reliability and longitudinal analysis of automated hippocampal subregion volumes in healthy ageing and Alzheimer's disease populations. Hum. Brain Mapp 39, 1743–1754 . [PubMed: 29341323]

Xu Y, Haacke EM, 2006. The role of voxel aspect ratio in determining apparent vascular phase behavior in susceptibility weighted imaging. Magn. Reson. Imaging 24, 155–160. [PubMed: 16455403]

Yablonskiy DA, Haacke EM, 1994. Theory of NMR signal behavior in magnetically inhomogeneous tissues: The static dephasing regime. Magn. Reson. Med 32, 749–763. [PubMed: 7869897]

Ye Y, Hu J, Wu D, Haacke EM, 2013. Noncontrast-enhanced magnetic resonance angiography and venography imaging with enhanced angiography. J. Magn. Reson. Imaging 38, 1539–1548. [PubMed: 23559486]
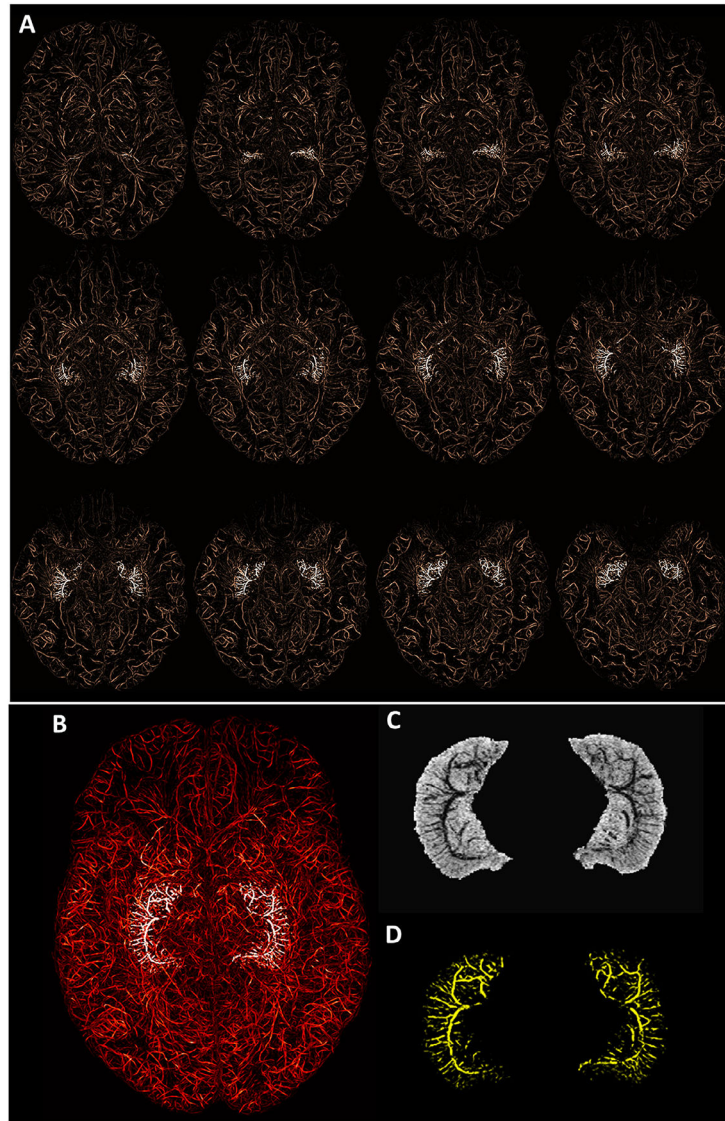
Fig. 1.
Mapping the micro-vasculature of the hippocampus using Ferumoxytol. A) The micro-vasculature map (MVM) segmented from SWI_{PGAC} using the vessel enhancing vesselness filter, overlaid with the highlighted hippocampal vessels (in white). The images are maximum intensity projected (MIP) over 9 mm (using a sliding window of 1 slice or 1mm) for visualizing the continuity of the vessels. B) The whole brain and highlighted hippocampal vessels MIPed over the entire coverage of the hippocampus (32 mm in this subject, 23-year-old, female). The minimum intensity projection (mIP) is shown in C) $SWI_{avg,2,3}$ data and the MIP in D) for all the segmented hippocampal vessels. The images in (c) and (D) have the same effective thickness as (B), which was set to 32 mm.
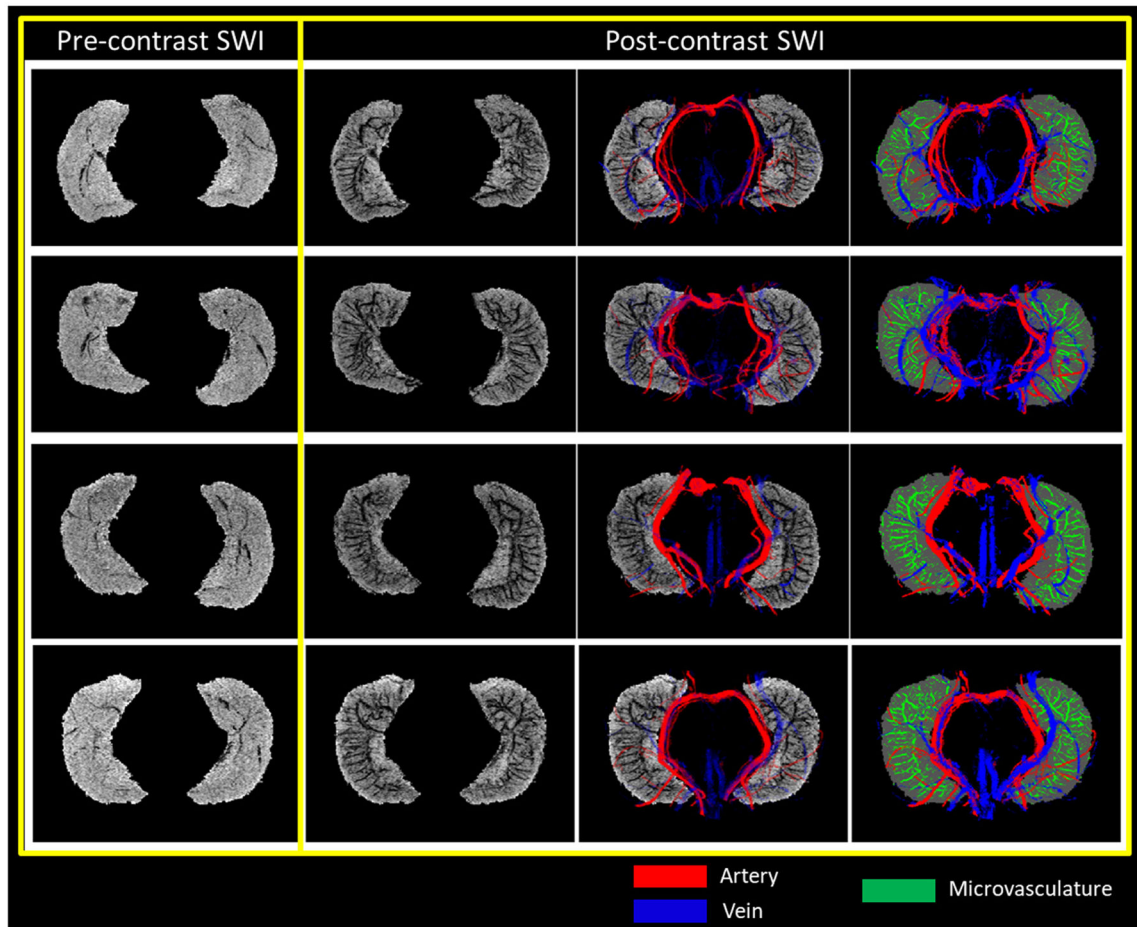
Fig. 2.
Segmenting the macro- and micro-vasculature of the hippocampus using pre- and post-contrast data. Pre-contrast SWI and SWI_{PGAC} data, for four healthy subjects (each in a row), are displayed with the overlays of major arteries (red), obtained from the MRA_{nl}, major veins (blue), obtained from MRV_{avg}, and intra-hippocampal micro-vasculature map or MVM (green). Although the pre-contrast SWI was able to highlight the presence of major veins due to the presence of deoxyhemoglobin, the vascular contrast was improved significantly on the post-contrast SWI data. The slice-by-slice visualization of the MRA_{nl}, MRV_{avg}, SWI_{PGAC}, the derived MVM and subfield segmentations are displayed in Figure S6.
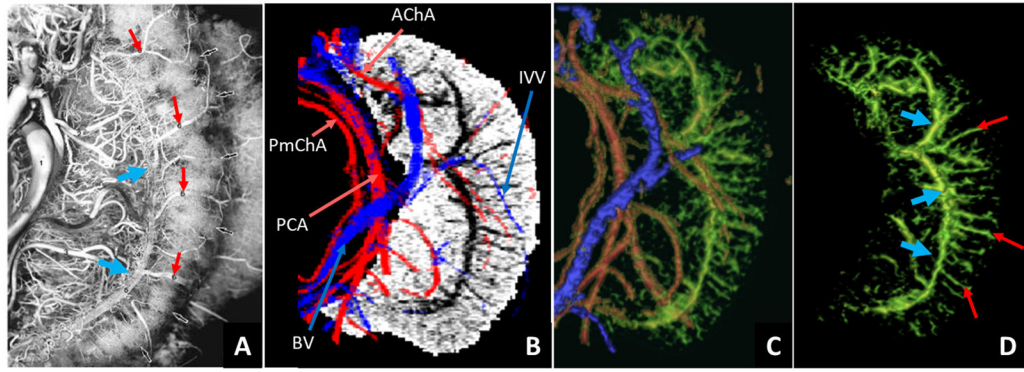
Fig. 3.

Comparison of the hippocampal vessels enhanced using the MICRO SWI data with cadaver brain data. A) Figure from a cadaver study on hippocampal vascularization using the vascular ink injection technique (Duvernoy et al., 2013) (adapted with permission from Springer Nature, The Human Hippocampus by Henri M. Duvernoy, copyright Springer-Verlag Berlin Heidelberg); B) mIP of the *in vivo* SWI$_{PGAC}$ data with the overlays of major arteries (red) and major veins (blue); C) the combined 3D rendering of the major arteries, major veins and the intra-hippocampal micro-vasculature (green); and D) the isolated hippocampal micro-vasculature showing agreement with the cadaver brain data in visualizing the fimbrio dentate sulcus (blue arrows) and the subependymal intra-hippocampal veins (red arrows). Major arteries: AChA = anterior choroidal artery; PCA = posterior cerebral artery; PmChA = posterior-medial choroidal artery; Major veins: BV = basal vein; IVV = inferior ventricular vein.
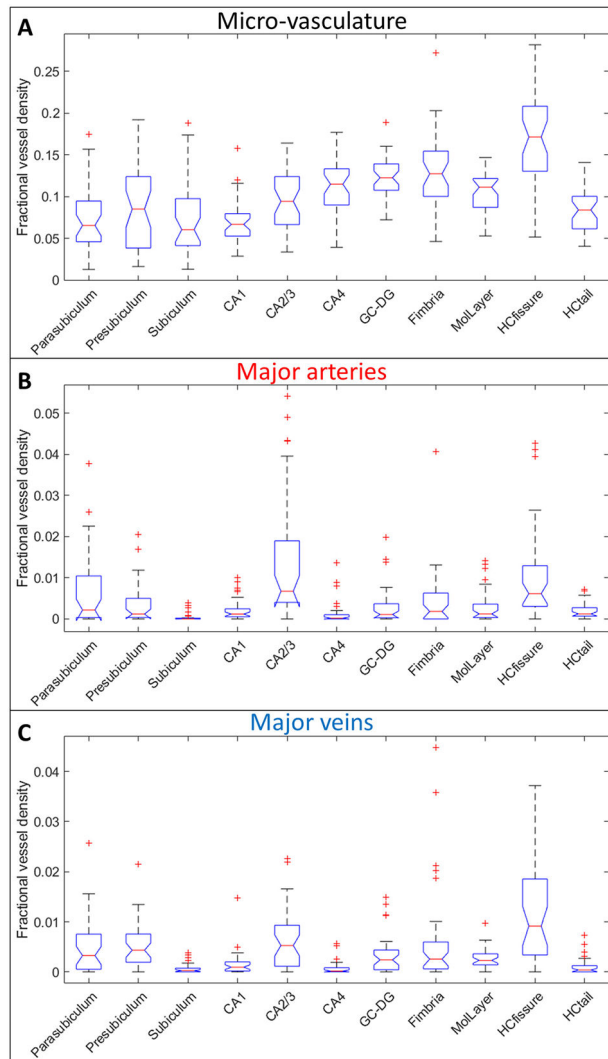
Fig. 4.
Boxplots of fractional vessel density (FVD) measures for the intra-hippocampal (A) micro-vasculature, (B) major arteries (using MRA_{nl}) and (C) major veins (using MRV_{avg}) for each of the subfields. The boxplots provide the median values in form of red lines, boxes across the interquartile range, and dotted bars across the 95% confidence interval regions. The significance in the differences across the various subfields are shown in Table S1. The values outside of this window are deemed as outliers and are plotted here as red + 's. CA1, CA2/3, CA4 = Cornu Ammonis layers, GC-DG = Granule cell layer of the dentate gyrus, MolLayer = Molecular layer of hippocampus, HCfissure = hippocampal fissure, HCtail = hippocampal tail.
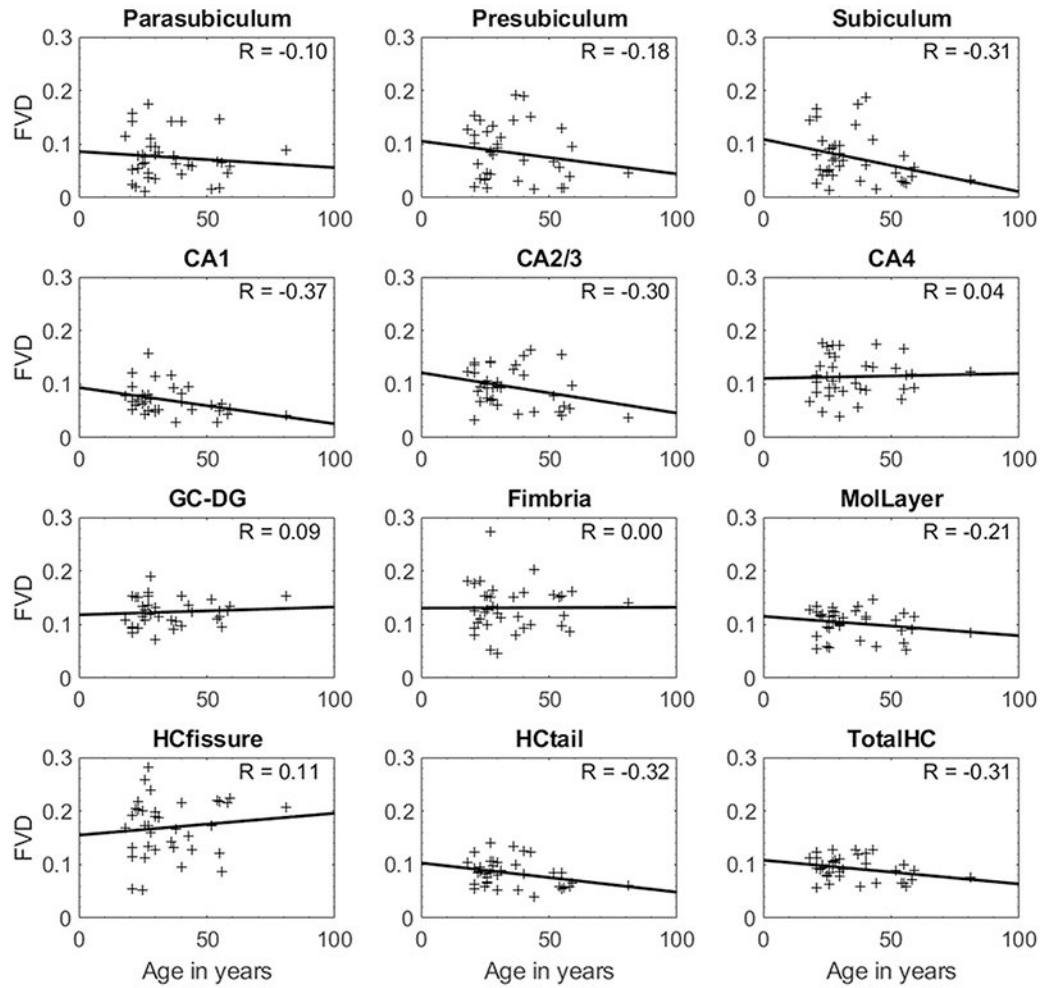
Fig. 5.
Age-dependent changes in the FVD for each hippocampal subfield and the FVD for the entire hippocampus (TotalHC). Pearson correlation coefficients (R) for each case are indicated on the top-left section of the plots. Out of all the subfields, CA1 exhibited a significant negative and moderate correlation ($R = -0.37$, $p = 0.024$) with age. CA1, CA2/3, CA4 = Cornu Ammonis layers, GC-DG = Granule cell layer of the dentate gyrus, MolLayer = Molecular layer of hippocampus, HCfissure = hippocampal fissure, HCtail = hippocampal tail.

Table 1

Mean ± inter-subject variability (ISV) of the FVD measures for the individual hippocampal subfields along with the FVD of the whole hippocampus (Total HC).

	Mean ± ISVMicro-vascular FVD	Micro-vascular FVD vs. age	
		R	p
Parasubiculum	0.073±0.04	−0.105	0.538
Presubiculum	0.084±0.05	−0.178	0.291
Subiculum	0.072±0.04	−0.311	0.061
CA1	0.067±0.03	−0.371	**0.024**
CA2/3	0.095±0.04	−0.300	0.071
CA4	0.114±0.04	0.036	0.831
GC-DG	0.121±0.03	0.085	0.616
Fimbria	0.127±0.04	0.005	0.977
MolLayer	0.103±0.03	−0.206	0.222
HCfissure	0.169±0.05	0.111	0.513
HCtail	0.084±0.02	−0.316	0.057
Total HC	0.093±0.02	−0.310	0.062

Pearson's correlation coefficient (R), along with its p-value, are listed for the individual subfields and for the total hippocampus as a function of age. CA1, CA2/3, CA4 = Cornu Ammonis layers, GC-DG = Granule cell layer of the dentate gyrus, MolLayer = Molecular layer of hippocampus, HCfissure = hippocampal fissure, HCtail = hippocampal tail.